8-1-2015

Confirming HD 23478 As A New Magnetic B Star Hosting An Hα-Bright Centrifugal Magnetosphere

J. Sikora

G. A. Wade

D. A. Bohlender

See next page for additional authors

Authors

J. Sikora, G. A. Wade, D. A. Bohlender, C. Neiner, M. E. Oksala, M. Shultz, David H. Cohen, A. ud-Doula, J. Grunhut, D. Monin, S. Owocki, V. Petit, T. Rivinus, and R. H. D. Townsend

Confirming HD 23478 as a new magnetic B star hosting an Hα-bright centrifugal magnetosphere

J. Sikora,[1,2]★ G. A. Wade,[2] D. A. Bohlender,[3] C. Neiner,[4] M. E. Oksala,[4]
M. Shultz,[1,2,5] D. H. Cohen,[6] A. ud-Doula,[7] J. Grunhut,[8] D. Monin,[3] S. Owocki,[9]
V. Petit,[10] T. Rivinus[5] and R. H. D. Townsend[11]

[1]*Department of Physics, Engineering Physics & Astronomy, Queen's University, Kingston, ON K7L 3N6, Canada*
[2]*Department of Physics, Royal Military College of Canada, PO Box 17000 Kingston, ON K7K 7B4, Canada*
[3]*Herzberg Astronomy and Astrophysics, National Research Council of Canada, 5071 West Saanich Road, Victoria, BC V9E 2E7, Canada*
[4]*LESIA, Observatoire de Paris, CNRS UMR 8109, UPMC, Université Paris Diderot, 5 place Jules Janssen, F-92195 Meudon Cedex, France*
[5]*ESO – European Organization for Astronomical Research in the Southern hemisphere, Castilla 19001, Santiago 19, Chile*
[6]*Department of Physics & Astronomy, Swarthmore College, Swarthmore, PA 19081, USA*
[7]*Penn State Worthington Scranton, Dunmore, PA 18512, USA*
[8]*European Organization for Astronomical Research in the Southern hemisphere, Karl-Schwarzschild-Str. 2, D-85748 Garching bei München, Germany*
[9]*Bartol Research Institute, University of Delaware, Newark, DE 19716, USA*
[10]*Department of Physics & Space Sciences, Florida Institute of Technology, Melbourne, FL 32901, USA*
[11]*Department of Astronomy, University of Wisconsin–Madison, 2535 Sterling Hall, 475 N Charter Street, Madison, WI 53706, USA*

ABSTRACT

In this paper, we report 23 magnetic field measurements of the B3IV star HD 23478: 12 obtained from high-resolution Stokes V spectra using the ESPaDOnS (Canada–France–Hawaii Telescope) and Narval (Télescope Bernard Lyot) spectropolarimeters, and 11 from medium-resolution Stokes V spectra obtained with the DimaPol spectropolarimeter (Dominion Astronomical Observatory). HD 23478 was one of two rapidly rotating stars identified as potential 'centrifugal magnetosphere' hosts based on IR observations from the Apache Point Observatory Galactic Evolution Experiment survey. We derive basic physical properties of this star including its mass ($M = 6.1^{+0.8}_{-0.7}\,\mathrm{M}_\odot$), effective temperature ($T_{\mathrm{eff}} = 20 \pm 2\,\mathrm{kK}$), radius ($R = 2.7^{+1.6}_{-0.9}\,\mathrm{R}_\odot$), and age ($\tau_{\mathrm{age}} = 3^{+37}_{-1}\,\mathrm{Myr}$). We repeatedly detect weakly variable Zeeman signatures in metal, He, and H lines in all our observations corresponding to a longitudinal magnetic field of $\langle B_z \rangle \approx -2.0\,\mathrm{kG}$. The rotational period is inferred from *Hipparcos* photometry ($P_{\mathrm{rot}} = 1.0498(4)\,\mathrm{d}$). Under the assumption of the Oblique Rotator Model, our observations yield a surface dipole magnetic field of strength $B_d \geq 9.5\,\mathrm{kG}$ that is approximately aligned with the stellar rotation axis. We confirm the presence of strong and broad Hα emission and gauge the volume of this star's centrifugal magnetosphere to be consistent with those of other Hα emitting centrifugal magnetosphere stars based on the large inferred Alfvén to Kepler radius ratio.

Key words: stars: early-type – stars: individual: HD 23478 – stars: magnetic field – stars: rotation – stars: winds, outflows.

1 INTRODUCTION

Upon the first detection of its magnetic field, the strong, broad, and variable Hα emission line of the main sequence B2 star σ Ori E was suggested to be a natural consequence of a plasma corotating with the star well beyond its surface (Landstreet & Borra 1978). Since then, a significant number ($\gtrsim 13$) of magnetic mid- to early-B stars (i.e. $T_{\mathrm{eff}} < 25\,\mathrm{kK}$) exhibiting Hα emission were discovered (Brown, Shore & Sonneborn 1985; Shore et al. 1990). These stars are of

particular interest because they provide a unique means of probing the mass-loss and stellar winds of B-type stars. While the strength of the magnetic field likely plays an important role in determining if a magnetic B star exhibits Hα emission, the key distinction between the stars with emission and those without is rotation – the emission line stars are all rapid rotators having rotational periods $\lesssim 1.5\,\mathrm{d}$ (Petit et al. 2013).

These correlations between rotation and the presence of Hα emission can be understood in a general framework in which the magnetospheres of massive stars are classified as either dynamic magnetospheres (DM) or centrifugal magnetospheres (CM) based

★E-mail: james.sikora@queensu.ca

Table 1. Observations of HD 23478 obtained with ESPaDOnS and Narval. The phases are calculated using equation (1). SNRs per 1.8 km s^{-1} spectral pixel are reported at 5400 Å. The three rightmost columns list the longitudinal magnetic field measurements obtained from Hβ and LSD profiles generated from a He+metal line mask along with the detection status according to the criteria of Donati et al. (1997): definite detection (DD), marginal detection (MD), and no detection (ND) (see Section 5).

HJD	Phase	Total exp. time (s)	SNR (pix^{-1})	Instrument	$\langle B_z \rangle_{H\beta}$ (kG)	$\langle B_z \rangle_{He + metal}$ (kG)	Detection status
2456884.116	0.304	560	473	ESPaDOnS	-1.52 ± 0.27	-1.98 ± 0.25	DD
2456908.146	0.194	560	500	ESPaDOnS	-1.68 ± 0.24	-2.15 ± 0.22	DD
2456909.134	0.135	560	381	ESPaDOnS	-1.42 ± 0.32	-2.33 ± 0.29	DD
2456909.144	0.145	560	346	ESPaDOnS	-1.89 ± 0.29	-2.26 ± 0.26	DD
2456925.512	0.736	1200	402	Narval	-2.19 ± 0.37	-1.98 ± 0.36	MD
2456925.691	0.907	1200	291	Narval	-2.32 ± 0.28	-2.49 ± 0.30	DD
2456962.025	0.517	560	409	ESPaDOnS	-0.95 ± 0.34	-1.93 ± 0.26	DD
2456968.937	0.101	560	409	ESPaDOnS	-2.13 ± 0.31	-2.44 ± 0.27	DD
2456972.833	0.813	560	353	ESPaDOnS	-1.94 ± 0.39	-2.52 ± 0.37	MD
2456972.843	0.822	560	352	ESPaDOnS	-2.98 ± 0.41	-2.84 ± 0.37	MD
2456973.099	0.066	560	497	ESPaDOnS	-2.05 ± 0.27	-2.11 ± 0.22	DD
2457034.695	0.740	560	461	ESPaDOnS	-1.63 ± 0.29	-1.99 ± 0.27	MD

on the ability of the field to confine the wind and the degree of criticality of the stellar rotation (ud-Doula & Owocki 2002; Petit et al. 2013). Petit et al. (2013), and more recently Shultz et al. (2014), demonstrate that stars like σ Ori E are those with the largest magnetospheric volumes: those with the largest Alfvén radii combined with the smallest Kepler radii. Shultz et al. (2014) estimated that Hα emission is never observed for typical magnetic B stars with $R_A/R_K \lesssim 10$, while it is frequently observed in the spectra of stars with ratios above this threshold.

Recently, Eikenberry et al. (2014) identified two emission line B stars from near-infrared (nIR) spectra obtained in the context of the Apache Point Observatory Galactic Evolution Experiment survey: HD 345439 and HD 23478. They found that both stars exhibited strong and broad emission at all nIR H lines along with relatively large projected rotational velocities of ≈ 270 and 125 km s^{-1}, respectively. Although lacking any information about their magnetic fields, Eikenberry et al. (2014) concluded that the similarities between these stars and σ Ori E provided reasonable evidence for a magnetospheric origin of the observed nIR emission.

The principal aim of this study is to search for the presence of a magnetic field in the brightest of these two stars (HD 23478), and to test the hypothesis of Eikenberry et al. (2014) that it is similar to σ Ori E in that it also belongs to the more general class of Hα-emitting CM stars. In Section 2, we describe the spectropolarimetric observations used in this study. In Section 3, we estimate the physical parameters of HD 23478 using photometric data from the literature along with newly acquired high-resolution spectroscopy. We then analyse in Section 4 variability in *Hipparcos* epoch photometry in an attempt to infer the star's rotational period. In Section 5, we compute the longitudinal magnetic field and search for its variability. Section 6 discusses the spectral line emission and variability. In Section 7, we derive the stellar magnetospheric parameters. Finally, in Section 8 we evaluate our hypothesis for a CM origin of HD 23478's emission.

2 OBSERVATIONS

2.1 High-resolution spectropolarimetry

HD 23478 was observed during eight nights between 2014 August and 2015 January using the ESPaDOnS and Narval spec-

tropolarimeters installed at the Canada–France–Hawaii Telescope (CFHT) and Télescope Bernard Lyot, respectively. Both instruments have a resolving power of $R \simeq 65\,000$ acquiring spectra in circularly polarized light spanning the visible range of 3600–10 000 Å. The Heliocentric Julian Dates (HJDs), exposure times, and signal-to-noise ratios (SNRs) of these observations are listed in Table 1.

Each circular polarization observation consists of four subexposures which the Libre-ESpRIT pipeline (Donati et al. 1997) automatically reduces yielding the final Stokes *I* and *V* spectra. The majority of the observations (10 out of 12) were obtained with ES-PaDOnS using a total exposure time of 560 s. The remaining two observations were obtained with Narval during a single night using a total exposure time of 1200 s.

2.2 Medium-resolution Hβ spectropolarimetry

11 spectropolarimetric observations were also obtained using the dimaPol medium-resolution spectropolarimeter located at the Dominion Astronomical Observatory (DAO) from 2014 January to 2015 March. The instrument has a resolving power of $R \approx 10\,000$ and is optimized to acquire spectra over a wavelength range of 4700–5300 Å (Monin et al. 2012). The HJDs, exposure times, SNRs, and longitudinal magnetic field measurements derived from Hβ Stokes *V* profiles are listed in Table 2.

3 PHYSICAL PARAMETERS

3.1 SED fitting

Photometry spanning a wide range of wavelengths is available for HD 23478, thereby providing a means of constraining both the effective temperature and surface gravity. These observations include monochromatic Johnson *UBV* (Anderson & Francis 2012), 2MASS *JHK*s (Skrutskie et al. 2006), and *TD*1 ultraviolet (Thompson et al. 1978) photometric measurements. Short (SWP imager: 1150–1975 Å) and long (LWP imager: 1900–3125 Å) wavelength ultraviolet broad-band measurements were also recorded by the *International Ultraviolet Explorer* (*IUE*). The high-resolution ($\delta\lambda = 0.1$ Å) *IUE* data were rebinned at $\delta\lambda = 3$ Å using the prescription of Solano (1998) in order to increase the SNR per pixel. All of the observed magnitudes were converted to physical fluxes using

Table 2. Observations of HD 23478 obtained with dimaPol. The phases are calculated using equation (1) and the magnetic field measurements correspond to the longitudinal field derived from Hβ Stokes *V* observations.

HJD	Phase	Total exp. time (s)	SNR (pix^{-1})	$\langle B_z \rangle_{\mathrm{H}\beta}$ (kG)
2456680.700	0.537	5400	300	-1.78 ± 0.56
2456681.630	0.422	3000	250	-0.92 ± 0.72
2456963.734	0.146	3000	440	-1.62 ± 0.27
2456971.888	0.911	4800	400	-2.88 ± 0.36
2456972.802	0.782	4800	520	-1.82 ± 0.26
2456973.758	0.693	4800	430	-1.29 ± 0.41
2456974.846	0.731	4800	410	-1.37 ± 0.38
2456976.032	0.859	4800	400	-2.08 ± 0.29
2456991.962	0.033	4800	480	-1.95 ± 0.30
2456992.711	0.748	4800	310	-1.86 ± 0.49
2457085.723	0.347	4800	550	-1.11 ± 0.33

published zero-points for Johnson and 2MASS filters (Bessell 1979; Cohen, Wheaton & Megeath 2003); both *TD*1 and *IUE* measurements were obtained in the appropriate units of ergs s^{-1} cm^{-2} Å^{-1}. Dereddening was applied using the method of Cardelli, Clayton & Mathis (1989) using a typical total-to-selective extinction of $R(V) \equiv A(V)/E(B - V) = 3.1$.

The photometric observations were compared with the non-local thermodynamic equilibrium (NLTE) TLUSTY BSTAR2006 synthetic energy distribution (SED) grid (Lanz & Hubeny 2007) for effective temperatures T_{eff} ranging from 15 to 30 kK and surface gravities $\log g$ (cgs) from 3 to 4.75. The published grid has T_{eff} and $\log g$ resolutions of 1000 K and 0.25, respectively, that were linearly interpolated to a finer grid of 250 K and 0.05 resolution. Solar abundances and a 2 km s^{-1} turbulence velocity were assumed for the model grid. The NLTE model SEDs have a resolution $\gtrsim 0.002$ Å – much higher than the rebinned *IUE* observations. We reduced the resolution of the model spectra by convolving with a Gaussian profile assuming a resolving power of $R = (1150\,\text{Å})/(3\,\text{Å}) \approx 380$ to match the 3 Å *IUE* bin-width at $\lambda = 1150$ Å. Theoretical monochromatic fluxes were calculated by convolving Johnson *UBV* and 2MASS *JHK*s transmission functions (Landolt & Uomoto 2007; Cohen et al. 2003) with the unbroadened model spectra.

The best-fitting NLTE model, shown in Fig. 1, was found to have an effective temperature, surface gravity, and colour excess of $T_{\mathrm{eff}} = 22.00$ kK, $\log g = 4.60$ (cgs), and $E(B - V) = 0.35$ yielding a reduced χ^2 value of 1.70. The monochromatic fluxes were found to be adequately reproduced by a wide range of T_{eff}, $\log g$, and $E(B - V)$ values. Changes in the surface gravity of each model SED were found to primarily affect the depths of the absorption lines, resulting in minimal changes in the calculated monochromatic fluxes. The *IUE* spectra provided the greatest constraint on the fitting parameters. In particular, we found relatively large discrepancies between the *IUE* LWP spectra and the model SEDs having $T_{\mathrm{eff}} \lesssim 20$ kK and $T_{\mathrm{eff}} \gtrsim 24$ kK at $2000 \lesssim \lambda \lesssim 2500$ Å. This is clearly a consequence of the respectively lower and higher values of the required extinction associated with these models. In Fig. 2, we show the LWP spectrum dereddened in order to fit models of 18, 20, 22, and 24 kK. The 2000–2500 Å region shows growing discrepancies for the lower and higher temperatures. This leads us to prefer $T_{\mathrm{eff}} = 22$ kK based on the SED fitting.
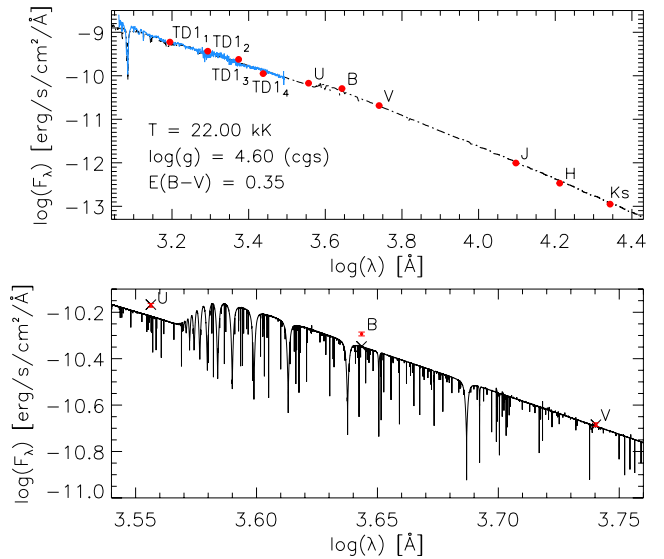

Figure 1. Top: comparing the *IUE* spectra (solid blue) and monochromatic fluxes (red points) with the best-fitting TLUSTY model (dashed black) convolved by a Gaussian profile to match the rebinned *IUE* resolution. Bottom: theoretical *U*, *B*, and *V* fluxes (black crosses) were calculated by convolving the unbroadened TLUSTY models (solid black) with the filter's associated transmission functions.
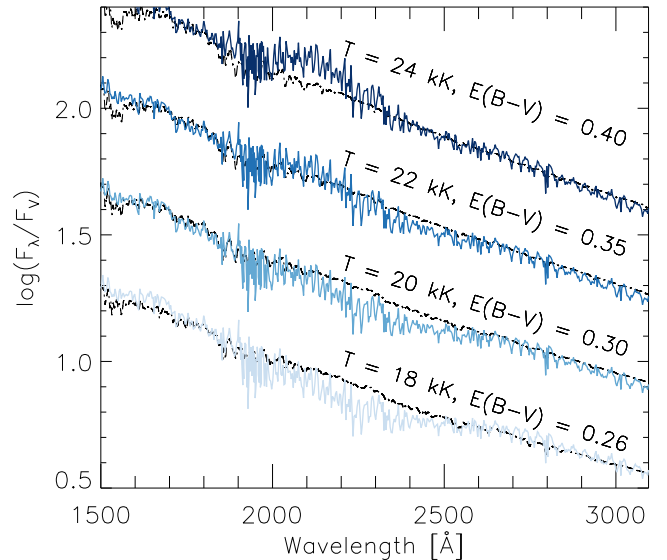

Figure 2. Comparisons between the *IUE* LWP spectrum (solid blue) and model SEDs (dashed black) at various effective temperatures and colour excesses. Both the models and the observations are normalized to the *V* flux (F_V).

3.2 Spectral line fitting

Spectral line fitting can provide a further constraint on T_{eff} and $\log g$ through comparisons between the obtained ESPaDOnS and Narval spectra and synthetic model grids. We found that HD 23478's metallic line spectrum was not suitable for tuning the atmospheric parameters due to a number of characteristics. The strongest metal lines have shallow depths of less than 10 per cent of the continuum with only three lines deeper than 5 per cent. This difficulty was alleviated to some extent by using averaged spectra thereby increasing the SNR by a factor of ≈ 3.5.
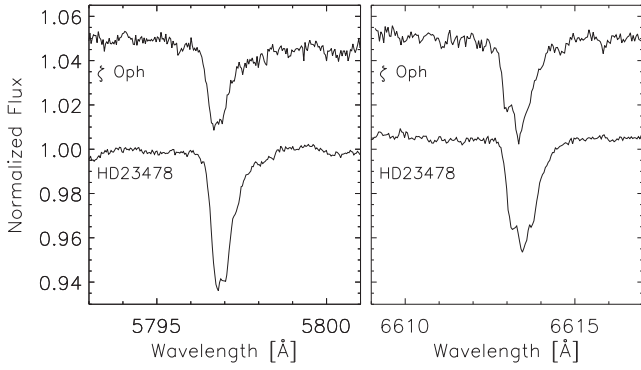
Figure 3. Comparisons between two DIBs found in the spectra of HD 23478 and ζ Oph.

We also noticed that many line profiles were distorted. Sharp asymmetric features having depths $\lesssim 10$ per cent of the continuum are prevalent in many spectral orders (Fig. 3). These were identified as diffuse interstellar bands (DIBs) by conferring with Hobbs et al. (2008, 2009) and by directly comparing the spectra of HD 23478 and ζ Oph, a star which is well known to exhibit strong DIB features (e.g. Walker, Bohlender & Krełowski 2000).

In addition to the DIB features, many metal lines show peculiar strengths and distorted profiles, likely due to non-solar surface abundances and non-uniform distributions of the abundances of these elements. As a consequence, modelling the metallic spectrum to constrain the atmospheric parameters would require a detailed analysis which is outside the scope of this work. Therefore, we opted to model the Balmer lines to provide further constraint on $T_{\rm eff}$ and $\log g$ because they are more weakly influenced by abundance non-uniformities. Specifically, Hγ and Hδ were chosen because of their relative insensitivity to emission (as compared to Hα) and because they are not directly adjacent to other strong absorption features, thus reducing normalization errors.

We relied primarily upon spectral models calculated using SYN-PLOT, the IDL wrapper for SYNSPEC (Hubeny & Lanz 2011), along with NLTE TLUSTY model atmospheres (Lanz & Hubeny 2007). The grid was linearly interpolated such that a finer resolution of $\delta T_{\rm eff} = 250$ K and $\delta \log g = 0.1$ (cgs) was obtained. The synthetic spectra
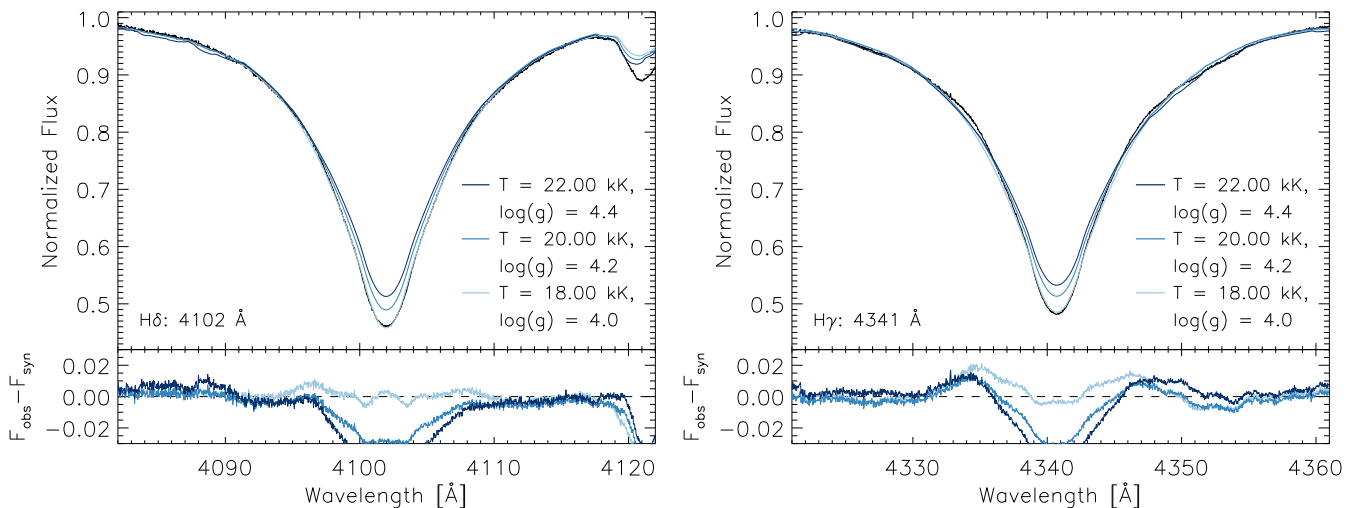
were then convolved with a Gaussian profile associated with the characteristic $R = 65\,000$ resolving power of the ESPaDOnS and Narval spectropolarimeters, corresponding to a velocity resolution of $\delta v \approx 4.6\,{\rm km\,s^{-1}}$. It is noted that changes in the He abundance can affect the wings of the Balmer lines (Leone & Manfre 1997). When calculating the NLTE H line profiles, we use the minimum He abundance of [He/H] $= -0.58$ required to fit a sample of averaged He I lines (where [He/H]$_\odot = -1.01$; Grevesse, Noels & Sauval 1996).

As shown in Fig. 4, the best effective temperature according to the SED fitting (22 kK) reproduces the Balmer line wings reasonably well with $\log g = 4.4$. However, the core depths are seriously underestimated by the model. By reducing $T_{\rm eff}$, good agreement between the observed and computed wings and core is achieved for $T_{\rm eff} = 18$ kK and $\log g = 4.0$.

We therefore find that the Balmer lines and SED yield different solutions to the atmospheric parameters. Based on our analysis, we conclude that the effective temperature of HD 23478 is likely in the range 18–22 kK and its surface gravity between 4.0 and 4.5. Further refinement of these parameters will require a more detailed future analysis.

The colour excess of $E(B - V) = 0.30^{+0.05}_{-0.04}$ inferred for the $T_{\rm eff} = 20 \pm 2$ kK range is in agreement with both the 0.28 and 0.34 values reported (without consideration of uncertainties) by Voshchinnikov et al. (2012) and Beeckmans & Hubert-Delplace (1980). For $T_{\rm eff} = 22$ kK however, a slightly higher $E(B - V) = 0.35$ is required. As was expected, $T_{\rm eff}$ was indeed found to be closely coupled with the colour excess.

3.2.1 Rotational broadening

To estimate the rotational broadening, we compared observed phase-averaged He and metal profiles with synthetic profiles computed assuming $T_{\rm eff} = 22$ kK. We adjusted the projected rotational velocity, $v \sin i$, as well as the abundance of each element in order to obtain a reasonable fit to the line profiles. Generally, a $v \sin i$ of $140 \pm 10\,{\rm km\,s^{-1}}$ yielded the best overall fit to the line profiles (consistent with that of Eikenberry et al. 2014). Fits to selected lines for several $v \sin i$ values are shown in Fig. 5. The inclusion of either macroturbulent or microturbulent broadening did not significantly
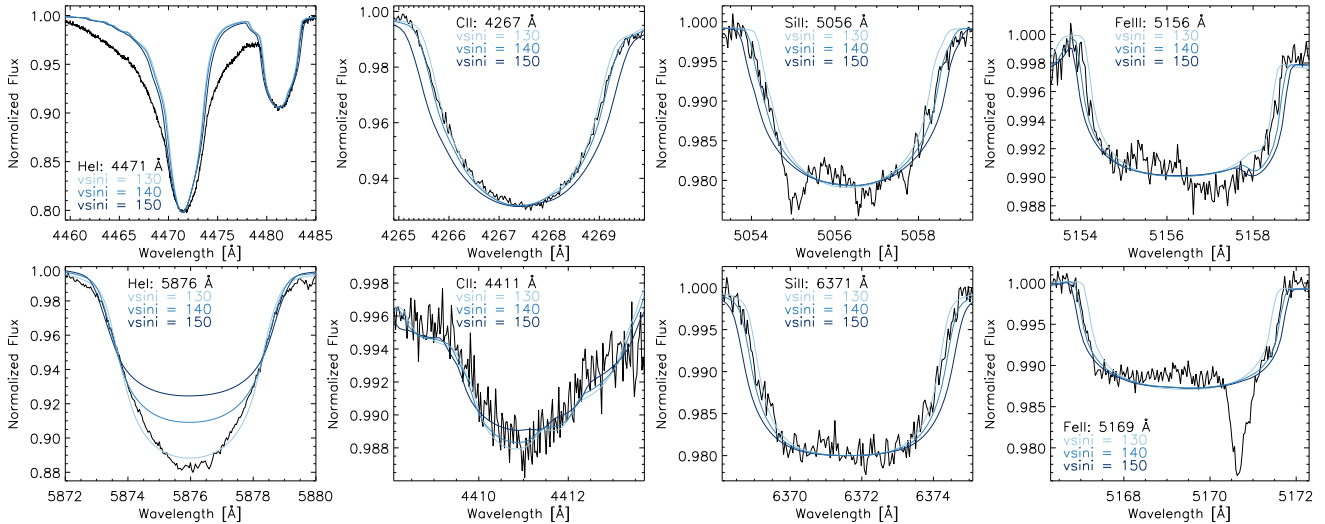

Figure 4. Comparisons between TLUSTY models (blue) and the averaged observed spectrum (black) for Hδ (left) and Hγ (right). The bottom frames show the residuals between the observations and the synthetic spectra ($F_{\rm obs} - F_{\rm syn}$).

Figure 5. $T_{eff} = 22$ kK and $\log g = 4.4$ TLUSTY models with a range of $v\sin i$ values compared with the averaged observed spectrum (black). The abundances of each element were adjusted in order to yield the best overall fit to the synthetic spectra. DIBs in both the Si II $\lambda 5056$ and Fe II $\lambda 5169$ lines are visible at 5055 and 5170.5 Å.

improve the fits. The distorted shapes of many line profiles are apparent. We also note the remarkably poor fit to the He I $\lambda 4471$ line. This discrepancy cannot be relieved by changing T_{eff} or $\log g$. It is reproduced in a number of other He I lines. We suspect that it is a consequence of stratification of He in the atmosphere of this star (e.g. Bohlender 1989; Farthmann et al. 1994).

3.3 Hertzsprung–Russell Diagram

The mass and age of HD 23478 were estimated by comparing its location on the Hertzsprung–Russell diagram (HRD) with theoretical isochrones and evolutionary tracks.

The luminosity of HD 23478 required to determine its location on the HRD was calculated using the dereddened visual magnitude of $V = 5.62^{+0.01}_{-0.07}$ mag where the colour excess of $E(B - V) = 0.30$ discussed in Section 3.2 was used. The calculation of the absolute visual magnitude, M_V, required a bolometric correction which was approximated by the temperature and surface gravity relation by Nieva (2013) applicable to stars with $15.8 \leq T_{eff} \leq 34.0$ kK. The luminosity was then found to be $L = 1.0^{+0.7}_{-0.4} \times 10^3 \, L_\odot$ where the primary contributions to the uncertainty are from the temperature (through the BC calibration) and parallax (i.e. the distance). The temperature of $T_{eff} = 20 \pm 2$ kK yielded by the SED fitting was used in the final HRD placement.

The comparisons used Geneva model grids of isochrones ranging in stellar age from 3.16 Myr to 12.9 Gyr generated by Ekström et al. (2012). The associated grid of evolution tracks contains models ranging in mass from 0.8 to 120 $M_\odot$; both the isochrone and evolution grids assume a solar metallicity of $Z = 0.014$. An identical resolution, $Z = Z_\odot$ grid which included rotational effects for a star having $v/v_{crit} = 0.4$ (Georgy et al. 2013) was also used in the analysis. However, the comparisons between the derived mass and radius of HD 23478 using both the rotating and non-rotating model grids yielded negligible differences of less than 5 per cent.

The position of HD 23478 on the HRD is shown in Fig. 6 where the nearby stellar evolution tracks are shown as dotted black lines and the main-sequence masses are indicated by black 'plus' symbols. The isochrones (indicated by red dotted lines), $\log L$, and $\log T_{eff}$ imply a range in the estimated age and radius
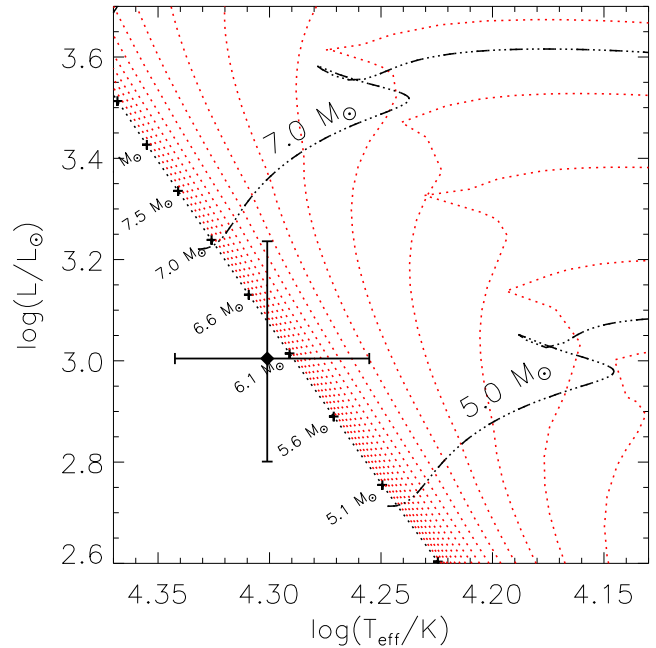

Figure 6. The position of HD 23478 is indicated by the black diamond. The evolutionary tracks (black dot–dashed lines) and isochrones (red dotted lines) assume a non-rotating star of solar metallicity (Ekström et al. 2012).

for the star of $\tau = 3^{+37}_{-1}$ Myr and $R = 2.8^{+1.3}_{-0.2}$, $R_\odot$, respectively. Likewise, the main-sequence mass of HD 23478 is estimated to be $M = 6.1^{+0.8}_{-0.7} \, M_\odot$. A similar radius of $R = 2.7^{+1.6}_{-0.9}$, $R_\odot$ is derived from L and T_{eff} using the Stefan–Boltzmann law; we adopt this value because of its larger uncertainty. We note that these mass and radius estimates imply a surface gravity of $\log g = 4.3^{+0.5}_{-0.4}$ which is consistent with the value derived from the spectral line fitting procedure described in Section 3.2.

4 ROTATIONAL PERIOD

The *Hipparcos* Epoch Photometry catalogue (Perryman et al. 1997) contains 75 measurements of HD 23478 spanning a time period of
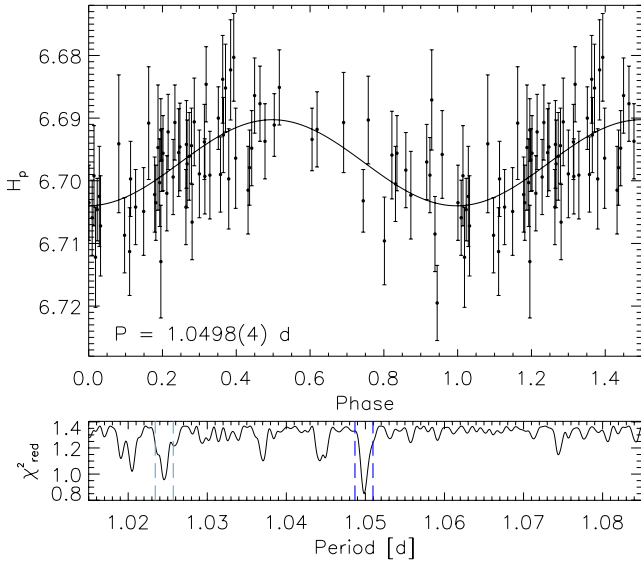
Figure 7. Top: *Hipparcos* Epoch Photometry phased with a period of 1.0498 d. Bottom: a subsample of the full reduced χ^2 versus period centred on the period of the best-fitting sinusoid. The 1.0498 d minimal-χ^2 solution is bounded by the dashed dark blue lines. The dashed light blue lines ($P_{rot} = 1.024\,54$ d) indicate the only other χ^2 peak falling below our chosen 3σ threshold.

Table 3. Stellar parameters of HD 23478.

Sp. type[1]	B3IV
π (mas)[2]	4.99 ± 0.62
d (pc)	200^{+29}_{-22}
Photometric	
V (mag)[3, 4]	$6.67^{+0.01}_{-0.07}$
$E(B - V)$ (mag)	$0.30^{+0.05}_{-0.04}$
BC (mag)	$-1.97^{+0.24}_{-0.22}$
M_V (mag)	$-0.77^{+0.26}_{-0.36}$
M_{bol} (mag)	$-2.74^{+0.51}_{-0.58}$
Physical	
T_{eff} (kK)	20 ± 2
$\log(g)$ (cgs)	4.2 ± 0.2
$v\sin i$ (kms^{-1})	140 ± 10
$\log L/L_{\odot}$	3.0 ± 0.2
$M/M_{\odot}$	$6.1^{+0.8}_{-0.7}$
$R/R_{\odot}$	$2.7^{+1.6}_{-0.9}$
τ_{age} (Myr)	3^{+37}_{-1}
P_{rot} (d)	1.0498 ± 0.0004
v_r (kms^{-1})	17 ± 5

References: [1]Blaauw & van Albada (1963), [2]van Leeuwen (2007), [3]Syfert, Hardie & Grenchik (1960), [4]Harris (1956).

three years with minimum and maximum time separations of approximately 20 min and 174 d, respectively. The measurements are therefore sufficient for detecting photometric variability across a wide range of time-scales associated with, for example, stellar rotation. All of the uncertainties are reported to be between 0.005 and 0.011 mag with a mean value of 0.007. Out of the 75 observations, three report the presence of anomalous measurements between the FAST and NDAC Data Reduction Consortia. Furthermore, one observation reports a magnitude that is $2.7\langle\sigma_{H_p}\rangle$ larger than $\langle H_p \rangle$ and is likely an outlier. The exclusion of any of the flagged or outlying data points had an insignificant effect on the estimated rotational period with a maximal deviation of $\Delta P < 5$ s.

The period of the Epoch Photometry observations was found by assuming a sinusoidal fit and calculating the reduced χ^2 distribution for periods ranging from 0 to 5 d with a resolution of $\delta P \sim 5$ s. This yielded a range of minimal-χ^2 solutions with the global minimum having a reduced χ^2 value of $\chi^2_{red} = 0.85$, occurring at a period of $P_{rot} = 1.0498$ d. The *Hipparcos* measurements phased at this best-fitting period are shown in Fig. 7 along with a subsample of the full periodogram centred on $P_{rot} = 1.0498$ d.

Assuming a 3σ confidence limit corresponding to an uncertainty of $\delta P = 0.0004$ d, we find that only one other period has a χ^2 value below this threshold at $P = 1.024\,54$ d where the χ^2 peak is shown in Fig. 7 (bottom) bounded by the dashed dark blue lines. The 1.024 54 d period does not result in a better fit compared with the 1.0498 d period; moreover, a similar analysis has previously been applied to ground-based photometry resulting in a photometric period of 1.0499 d (for which no uncertainty is reported) (Jerzykiewicz 1993). We therefore adopt the 1.0498 d period along with the ephemeris

$$JD = 244\,8700.606 \pm 1.0498(4) \times E, \qquad (1)$$

where the reference JD (244 8700.606) corresponds to the epoch of H_p maximum.

When phased with this ephemeris, the H_p data exhibit a roughly sinusoidal variation with a full amplitude of 0.015 mag and extrema located at phases of 0.00 ± 0.05 and 0.50 ± 0.05.

As discussed by Jerzykiewicz (1993), several possibilities exist for the origin of the 1.0498 d photometric period. Slowly pulsating B stars typically have periods $\sim$0.5–5.0 d and can be conclusively identified by the presence of multiperiodicity (Waelkens 1991). Jerzykiewicz (1993) noted that g-mode pulsations could potentially explain the observed variability. Another explanation is that HD 23478 is an eclipsing binary with a dimmer, less-massive companion for which no spectral signature is found. Jerzykiewicz (1993) rejected this possibility arguing that radial velocity variations $\gtrsim 80$ kms^{-1} would be exhibited in this scenario. The observations analysed here do not exhibit any variations ≥ 5 kms^{-1}.

Assuming that the photometric variations are instead caused by rotational modulation, the inclination angle of the stellar rotation axis, i, can be inferred from the projected rotational velocity, $v\sin i = 140 \pm 10$ kms^{-1}, and the stellar radius, $R = 2.7^{+1.6}_{-0.9}$ R$_{\odot}$, resulting in an inclination of $i = 69^{+21}_{-10}{}^{\circ}$ where the uncertainty is propagated from the 3σ value of $\delta P_{rot} = 0.0004$ d and estimated errors in R and $v\sin i$. These values imply a stellar rotational velocity of $v = 150^{+30}_{-20}$ kms^{-1} which is consistent with typical values for B stars (McNally 1965). Therefore, in agreement with Jerzykiewicz (1993), we conclude that the observed *Hipparcos* photometric variations are mostly likely generated by the star's rotation.

The physical parameters of HD 23478 derived in Section 3 along with its previously reported spectral type, parallax, and V magnitude are listed in Table 3.

5 MAGNETIC FIELD

The longitudinal magnetic field, $\langle B_z \rangle$, is measured through Zeeman signatures in the circularly polarized Stokes V spectrum. In order to maximize the SNR in these observations, the least squares

deconvolution (LSD) cross-correlation procedure (Donati et al. 1997; Kochukhov, Makaganiuk & Piskunov 2010) was applied to all ESPaDOnS and Narval spectra. The LSD line masks are constructed using spectral line lists associated with a specified surface gravity, effective temperature, detection threshold (i.e. the central depth of the weakest lines included in the mask), and microturbulence (v_{mic}) obtained from the Vienna Atomic Line Database (Piskunov et al. 1995). In the case of HD 23478, a detection threshold of 0.01 and $v_{mic} = 0$ were used. Terrestrial atmospheric absorption appears as deep, narrow telluric lines in the Stokes I LSD profiles that can significantly affect the value of $\langle B_z \rangle$; therefore, any lines near spectral regions where tellurics were present were removed.

$\langle B_z \rangle$ measurements are known to vary to some extent depending on which element's atomic absorption lines are used to analyse the Zeeman signatures (e.g. Pyper 1969; Bohlender et al. 1987; Yakunin et al. 2015). Several LSD line masks were therefore created in order to better evaluate the strength and variability of the inferred field – one which contained only He lines, one in which both H and He lines were removed leaving only absorption due to metals, and one containing both He and metal lines.

For each line mask, we adopted normalization values of the wavelength, Landé factor, and line depth of 500 nm, 1.2, and 0.2, respectively. Both the pure He and pure metal line masks yielded results similar to the combined He+metal line mask. This latter mask resulted in the smallest uncertainties. Examples of the Stokes V and I, and of the N (circularly polarized intensity, total intensity, and null diagnostic) LSD profiles obtained using the He+metal line mask at three phases are shown in Fig. 8. The profiles corresponding to phases of 0.140 and 0.817 were obtained by combining two consecutive measurements resulting in a moderately increased SNR.

The three LSD profiles shown in Fig. 8 demonstrate that no strong variability is observed in the He and metal line Zeeman signatures. We also computed the longitudinal magnetic field from each LSD profile using equation (1) of Wade et al. (2000) where an integration range of $v \in (-140, 170)\,\mathrm{km\,s^{-1}}$ was used. The values of $\langle B_z \rangle$ derived from the He+metal mask are reported in Table 1. We phased these measurements according to the photometric period of equation (1). The phased longitudinal field measurements calculated using the He+metal ($\langle B_z \rangle_{He+metal}$) LSD line mask are shown in Fig. 9.

Measurements of the longitudinal field were also determined using the core of the Hβ line. As with the measurements obtained from LSD profiles, the first moment method was applied. We integrated the ESPaDOnS and Narval Stokes V and I profiles across the full core, from -200 to $220\,\mathrm{km\,s^{-1}}$. Stokes I was normalized to the spectral flux computed from the 10 pixels located immediately outside the integration range. The process used to calculate the DAO longitudinal field measurements is outlined in Monin et al. (2012). The ESPaDOnS and Narval measurements are listed in Table 1 and the DAO measurements are listed in Table 2.

The phased Hβ longitudinal measurements ($\langle B_z \rangle_{H\beta}$) show a somewhat larger amplitude variation of 0.6 ± 0.1 kG compared with the 0.3 ± 0.1 kG amplitude obtained from the He+metal LSD profiles (Fig. 9).

While the sinusoidal fits to the two $\langle B_z \rangle$ data sets appear to reproduce the phased measurements reasonably well, only the variability observed in $\langle B_z \rangle_{H\beta}$ is statistically significant. Furthermore, the phases of the extrema of the sinusoidal fits (0.4–0.5 and 0.9–1.0 with uncertainties of about 0.05) are in agreement amongst the two curves. This suggests that the marginal detections of $\langle B_z \rangle_{He+metal}$ variations are in fact real.

In the context of the Oblique Rotator Model (ORM), periodic variations in $\langle B_z \rangle$ can be understood to be due to the rotation of a star
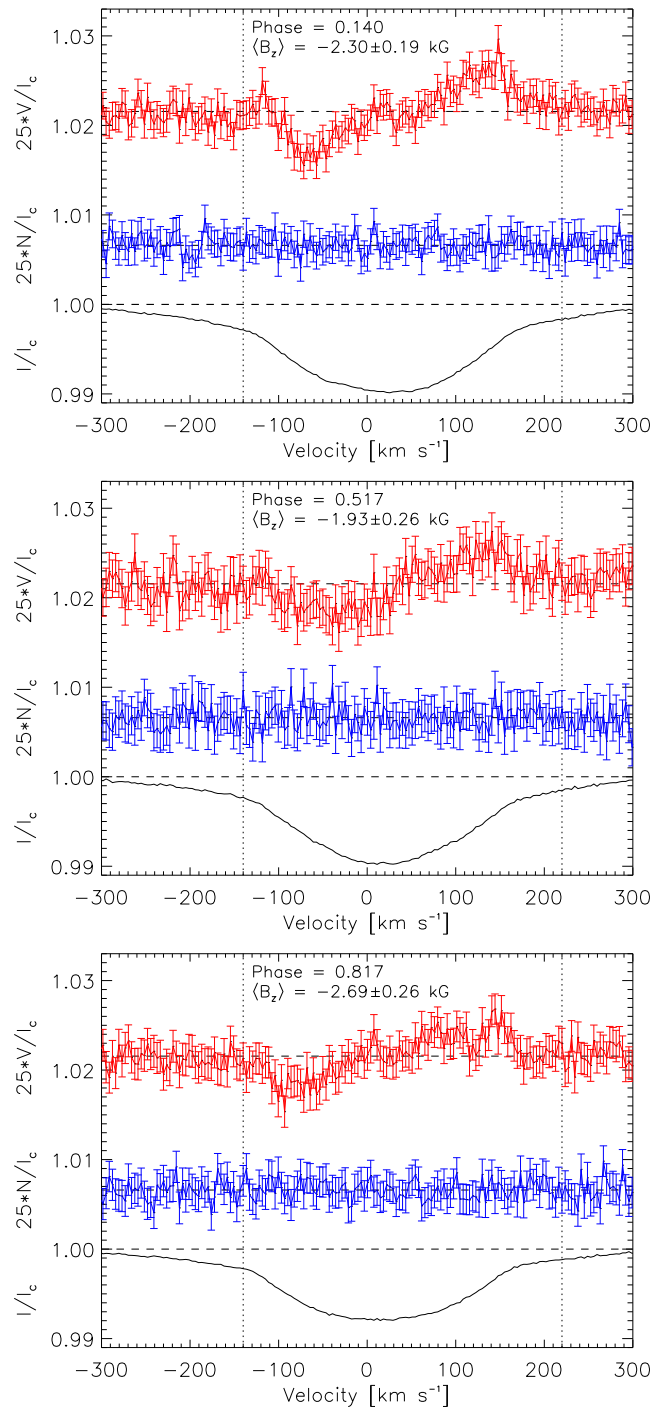

Figure 8. Examples of He+metal LSD profiles at three phases showing Zeeman signatures in Stokes V (top, red), along with associated Stokes I (bottom, black) and diagnostic null (middle, blue) profiles. Vertical dotted lines indicate the integration range.

having a dipolar magnetic field component with an axis of symmetry that is inclined from the rotational axis by an angle β (Stibbs 1950). Assuming that HD 23478's magnetic field is characterized by an important dipole component, as typically observed in hot stars, the faint variability observed in the $\langle B_z \rangle$ measurements shown in Fig. 9 implies an obliquity angle of $\beta \approx 0°$. Other explanations for the weak longitudinal field variability can be excluded based on the inferred rotational period and observed spectral properties. For
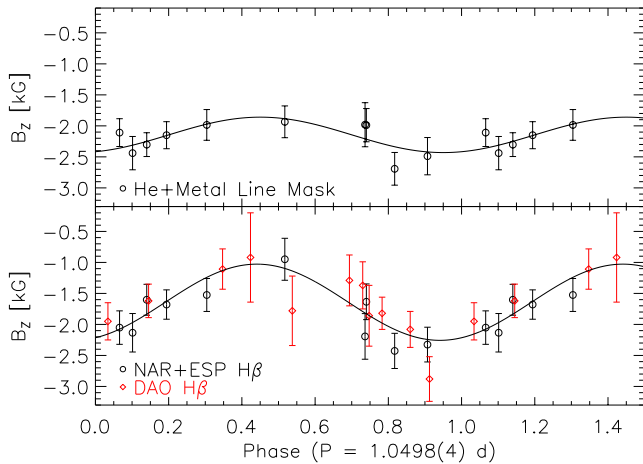
Figure 9. Longitudinal magnetic field measurements phased according to equation (1). The curves correspond to the best-fitting sinusoids. Top: $\langle B_z \rangle$ values derived using He+metal LSD line profiles. Bottom: $\langle B_z \rangle$ values derived from Hβ Stokes V observations. Black circles correspond to measurements obtained by Narval and ESPaDOnS while red diamonds are those obtained with dimaPol.

instance, regardless of the value of β, no variations in $\langle B_z \rangle$ would be apparent if $i = 0°$; however, this is inconsistent with the $i = 69^{+21°}_{-10}$ calculated in Section 4. Weak variability would also be observed if the star's rotational period is on the order of the observing time-scale of $\tau_{\rm obs} \gtrsim 30$ d. This is inconsistent with HD 23478's inferred 1.0498 d rotational period and relatively large $v \sin i$.

In the ORM, the obliquity angle is derived from i along with the best sinusoidal fit to the $\langle B_z \rangle$ measurements, given by $\langle B_z \rangle = B_0 + B_1 \sin 2\pi(\phi - \phi_0)$, using the relation given in equation (3) of Preston ([1967]). A least-squares analysis yielded the fit to $\langle B_z \rangle_{\rm He + metal}$ shown in Fig. [9], described by the parameters $B_0 = -2.1 \pm 0.1$ kG, $B_1 = 0.3 \pm 0.1$ kG, and $\phi_0 = -0.3 \pm 0.4$ where the uncertainties correspond to 1σ confidence. Applying equation (3) of Preston ([1967]) with the inclination angle derived above and $r = 0.77 \pm 0.12$ (equation 2 of Preston [1967]) results in an obliquity of $\beta = 3^{+4\circ}_{-3}$. A similar value of $8° \pm 8°$ was found for $\langle B_z \rangle_{\rm H\beta}$.

With the inclination and obliquity angles known, the polar strength of the surface dipole component of the magnetic field can be estimated using the method of Preston ([1967]). For this calculation, we use a maximum longitudinal field magnitude of $|\langle B_z \rangle^{\rm max}| = 2.4 \pm 0.2$ kG as given by the sinusoidal fit to $\langle B_z \rangle_{\rm He + metal}$ and a limb-darkening coefficient determined by linearly interpolating the values associated with the TLUSTY model atmosphere grid yielding a value of $u = 0.398$ for the $T_{\rm eff} = 20$ kK, $\log g = 4.2$ model (Daszyńska-Daszkiewicz & Szewczuk [2011]). This yields a dipole field strength of $B_d \geq 12.0$ kG where no upper limit is provided due to the divergence of the dipole field as $\beta \rightarrow 0°$ and $i \rightarrow 90°$. A relatively small difference in the lower limit of B_d was found (9.5 kG) using the combined Narval, ESPaDOnS, and DAO $\langle B_z \rangle_{\rm H\beta}$ values. The results of the magnetic analysis are summarized in Table [4].

We note that an upper limit on the dipole field strength may be estimated based on the fact that Zeeman splitting is not observed in the spectral lines themselves. However, given the high $v \sin i$ of the star, those constraints are not likely to be very helpful. Moreover, the field strength may be better constrained by generating synthetic Stokes V profiles (e.g. Petit & Wade [2012]). On the other hand, its utility would likely be hampered by the weak variability of the Stokes V profiles. Such an analysis is beyond the scope of this work

Table 4. Calculated values of various parameters associated with the magnetosphere of HD 23478 as derived from He+metal LSD profiles and Hβ. For those values dependent on B_d, which diverges as $\beta \rightarrow 0°$ and $i \rightarrow 90°$, only lower limits are provided.

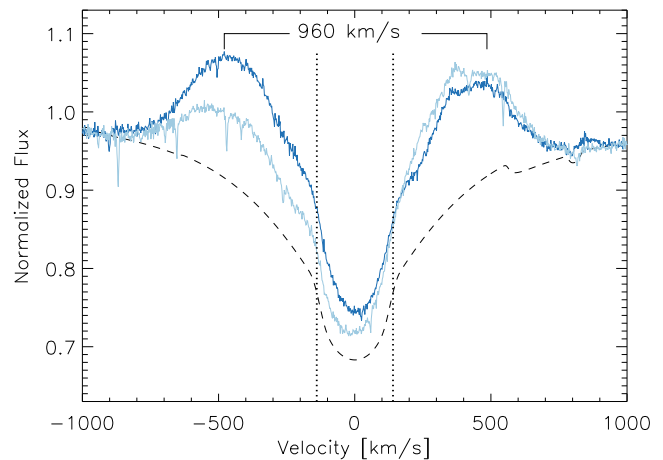|	He+metals$_{\rm LSD}$	Hβ
i (deg)	69^{+21}_{-10}	
$\dot{M}_{B=0}$ ($\times 10^{-10}$ M$_\odot$ yr^{-1})	$2.0^{+0.8}_{-0.4}$	
V_∞ ($\times 10^3$ km s^{-1})	$1.2^{+0.4}_{-0.3}$	
R_K (R_*)	$2.9^{+1.7}_{-1.2}$	
β (deg)	3^{+4}_{-3}	8 ± 8
B_d (kG)	≥ 12.0	≥ 9.5
η_*	$\geq 2.1 \times 10^5$	$\geq 1.3 \times 10^5$
$R_{\rm A}$ (R_*)	≥ 21.3	≥ 19.0
$R_{\rm A}/R_{\rm K}$	≥ 4.6	≥ 4.1

Figure 10. Maximum Hα emission (solid dark blue), as observed at a phase of 0.740, forms a double-horned peak separated by a velocity of ± 480 km s^{-1} well beyond the stellar surface indicated by the vertical dotted black lines at $v \sin i = \pm 140$ km s^{-1}. Minimum Hα (solid light blue) observed at a phase of 0.516. The dashed black curve is the $T_{\rm eff} = 22$ kK, $\log g = 4.4$ TLUSTY model spectrum discussed in Section 3.2.

but could be carried out in the future using a more extensive and higher SNR spectropolarimetric data set.

6 EMISSION AND VARIABILITY

HD 23478 was originally identified as a potential CM star based on the large degree of emission occurring at all nIR H lines (Eikenberry et al. [2014]). As expected, the most significant emission detected in the visible observations presented here occurs at the Hα line. Fig. [10] shows the minimum and maximum emission observed at phases of 0.740 and 0.516 and visible at all phases forming a double peak with a separation of approximately ± 480 km s^{-1}. The large Doppler-shifted velocities of the peaks are more than three times the star's projected rotational velocity of $v \sin i = 140 \pm 10$ km s^{-1} (indicated by the dotted vertical lines in Fig. [10]). If we assume that this emission is produced by gas bound in corotation with the star, this implies the presence of an emitting plasma at $R \gtrsim 3R_*$.

Although Hα presents the largest emission throughout the observed spectra, it varies relatively weakly (in comparison to σ Ori E, for example) over the 1.0498 d photometric period. This is
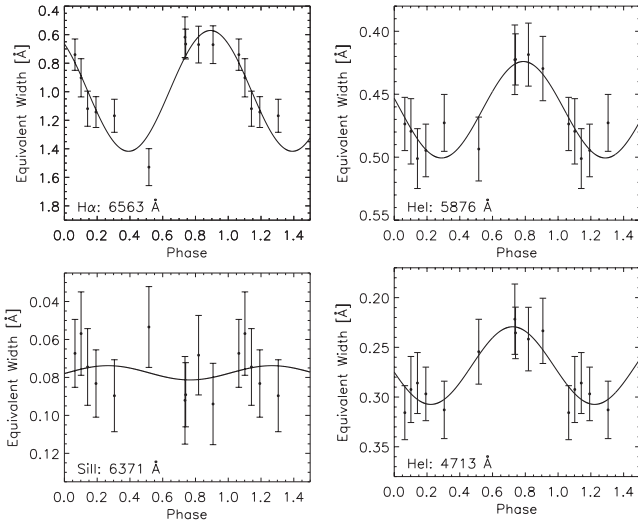
Figure 11. EWs of variable absorption lines phased with the star's rotational period of $P_{\rm rot} = 1.0498$ d.

demonstrated by the equivalent width (EW) measurements shown in Fig. 11 and the overplotted line profiles shown in Fig. 12. Similar to the ORM interpretation of a sinusoidally varying longitudinal magnetic field, the continuous and strong emission of CM stars is also expected to be rotationally modulated (e.g. Oksala et al. 2012). We find that the Hα EWs vary coherently when phased by the 1.0498 d period and is therefore consistent with this interpretation.

The clearest example of HD 23478's spectral variability is found in He line EW measurements as demonstrated by He I λ4713 and He I λ5876 shown in Fig. 11. While low SNRs and sparse phase coverage prevent an independent determination of $P_{\rm rot}$ from these EW variations, our observations are in agreement with a 1.0498 d period. Furthermore, Hα and the He lines do not vary coherently when phased by the other candidate 1.024 54 d rotational period discussed in Section 4. This provides further evidence in support of a 1.0498 d rotational period.

The maximum and minimum Hα EWs occur at phases 0.39 ± 0.05 and 0.89 ± 0.05, respectively. These values are ap-
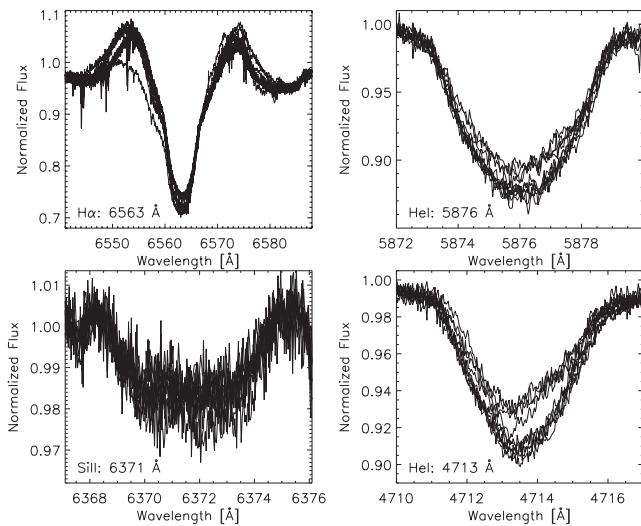

Figure 12. Overlayed line profiles associated with the EWs shown in Fig. 11 from each of the 12 measurements. Significant variability was found in all identified He I lines.

proximately in phase with both the *Hipparcos* photometry and the $\langle B_z \rangle$ measurements. The He I λ5876 and He I λ4713 EW measurements are in mutual agreement and have maximum and minimum values at 0.76 ± 0.06 and 0.26 ± 0.06. They are shifted in phase relative to H_p and $\langle B_z \rangle$ by 0.24 ± 0.08, i.e. one-quarter of one cycle.

7 MAGNETOSPHERE

The defining characteristic of CM stars aside from the often present strong and broad emission lines is their large ratio of the Alfvén radius to the Kepler co-rotation radius (Petit et al. 2013). The Kepler radius defines the point at which a rigidly rotating star's gravitational force is balanced by the outward centrifugal force. Based on HD 23478's inferred mass and rotational period, we calculate a Kepler radius of $R_K = 2.9^{+1.7}_{-1.2} R_\odot$. The Alfvén radius ($R_A$) can be estimated from the wind confinement parameter (η_*) which depends on the equatorial magnetic field magnitude ($B_{\rm eq}$), the stellar radius, mass-loss rate in the absence of a magnetic field ($\dot{M}_{B=0}$), and terminal wind speed (V_∞) as derived by ud-Doula, Owocki & Townsend (2008). Following the treatment carried out by Petit et al. (2013), we calculate η_* using the calibration for $\dot{M}_{B=0}$ derived by Vink, de Koter & Lamers (2000) with $V_\infty = 1.3 V_{\rm esc}$ for a $T_{\rm eff} = 20$ kK star.

Assuming the B_d values calculated in Section 5, we derived η_* and R_A based on the He+metal and Hβ analyses and find the results to be consistent. The larger uncertainties on the Hβ measurements yielded the lowest minimum η_* and R_A at 1.3×10^5 and $19.0 R_*$, respectively. With a Kepler radius of $R_K = 2.9^{+1.7}_{-1.2} R_\odot$, we obtain a ratio of $R_A/R_K = 13.3$ (with a lower limit of 4.6) thereby placing HD 23478 well within the CM star regime (i.e. those with $R_A/R_K > 1$). The full range of magnetospheric parameters calculated from $\langle B_{\rm He+metal} \rangle$ and $\langle B_{H\beta} \rangle$ are listed in Table 4.

In the context of all known CM stars, the estimated Kepler and Alfvén radii place HD 23478 within a region of the magnetic confinement diagram – fig. 3 of Petit et al. (2013) – populated by approximately 12 mid to early B-type stars. Six of these are reported to exhibit Hα emission and only one from this subset – HD 142990 – has a rotational period shorter than that of HD 23478 (Bychkov, Bychkova & Madej 2005). The lowest reported dipolar magnetic field strengths of these 12 CM stars is HD 176582's $B_p \geq 7.0$ kG, a Bp star that exhibits comparatively weaker Hα emission (Bohlender & Monin 2011).

We note that HD 23478 exhibits similar physical and spectral properties to the well-studied B2Vp star σ Ori E. σ Ori E has a comparable effective temperature of 23 ± 1 kK (Groote & Hunger 1982) and its rotational period and projected rotational velocity differ from HD 23478 by as little as 13 and 6 per cent, respectively (Townsend et al. 2010). Hα EW measurements of σ Ori E show stronger variability ∼3 Å (Oksala et al. 2012) compared with the $\Delta EW_{H\alpha} \sim 1$ Å derived for HD 23478. In terms of the empirical $R_A/R_K \gtrsim 10$ limit noted by Shultz et al. (2014) for the occurrence of Hα emission in CM-hosting stars, these differences in emission properties are consistent with σ Ori E's likely higher R_K/R_A of approximately 15 (Petit et al. 2013).

Comparisons with the rigidly rotating magnetosphere (RRM) model[1] (Townsend & Owocki 2005) suggest that the photometric variability of HD 23478 may be caused by variable occultation of the stellar disc by the magnetosphere. In this scenario, the

---

[1] For a visualization, see: www.astro.wisc.edu/townsend/static.php?ref=rrm-movies.

plasma forms a circumstellar disc in the magnetic equatorial plane. A non-zero obliquity may then allow the plasma to periodically eclipse the stellar disc resulting in an observed dimming of the star.

The Hα emission and unsigned longitudinal field ($|\langle B_z \rangle|$) associated with an $i = 70^\circ$ and $\beta = 10^\circ$ RRM model are predicted to be in phase; this is consistent with our analysis of HD 23478. This supports our interpretation of the emission and its variability as due to magnetically confined plasma in a CM. On the other hand, the model also predicts a maximum photometric brightness at the phase of maximum $|\langle B_z \rangle|$, whereas we observe roughly the opposite. Therefore, the periodic dimming of the star is likely not related to magnetospheric occultation.

Photometric variability may be observed if chemical spots are present on the star's surface, which serve to redistribute the star's flux into the UV (e.g. Peterson 1970; Krtička et al. 2013, 2015). The variable He line profiles introduced in Section 6 provide evidence for He spots on the surface of the star. However, the He EWs do not vary in phase with H_p but are instead shifted by one quarter of a cycle. Thus, He spots are also not able to fully account for the observed H_p variations. On the other hand, spots of other elements (in particular Si and Fe) may well also contribute. Such an investigation would be a useful element of a future, more detailed study of HD 23478.

8 CONCLUSIONS

Based on our analysis, we draw the following conclusions:

(i) HD 23478 is a main-sequence magnetic He-strong star ($T_{\rm eff} = 20 \pm 2$ kK) exhibiting peculiar line strengths and distorted line profiles of He, Si, and Fe, indicating likely non-uniform surface distributions of these elements;

(ii) the 1.0498(4) d period found in *Hipparcos* epoch photometry is most likely the star's rotational period which confirms the earlier findings of Jerzykiewicz (1993);

(iii) the presence of strong Hα emission is consistent with the discovery by Eikenberry et al. (2014) of emission in Hα and nIR H lines. This emission forms a double peaked profile separated by $v \approx 960$ km s^{-1} which likely originates from plasma located at a distance of $R > 3 R_*$. We observe significant variability in Hα and in various He lines. Measured EWs of these lines are coherently phased by $P_{\rm rot} = 1.0498$ d;

(iv) the surface magnetic field is inferred to have an important dipole component, with a minimum polar strength 9.5 kG, nearly aligned with the star's rotation axis.

Our results unambiguously imply the presence of a centrifugally supported, magnetically confined plasma around HD 23478, and therefore confirm the hypothesis of Eikenberry et al. (2014) that it is a member of the growing class of magnetic B stars hosting CMs.

Our analysis yielded a relatively significant discrepancy in the determination of the star's effective temperature. *IUE* spectra used in the SED modelling imply $T_{\rm eff} = 22$ kK while the observed Balmer lines require a lower temperature of 18 kK to provide the best fit. Chemical peculiarities, line profile distortions, and relatively weak and scarce metal lines prevent this ambiguity from being confidently resolved within the scope of this study.

The low inferred obliquity angle of $\beta \leq 16^\circ$ paired with the high $69^{+21}_{-10}{}^\circ$ inclination angle introduce basic uncertainties in modelling the star's magnetic field and magnetosphere. Consequently, only lower limits on the Alfvén to Kepler radius ratio and the magnetic field's dipole component were obtained. We find that the derived

$R_{\rm A}/R_{\rm K} \geq 4.1$ and $B_d \geq 9.5$ kG place HD 23478 within the more extreme subset of stars hosting CMs.

Future work is necessary to more precisely constrain the magnetic field topology, magnetospheric properties, and chemical peculiarities of this star. Although the class of strongly Hα-emitting stars hosting CMs is growing, the total number is still relatively low. Therefore, a detailed characterization of all known cases is important in order to better understand the interaction between magnetic fields and the winds of hot stars.

REFERENCES

Anderson E., Francis C., 2012, Astron. Lett., 38, 331
Beeckmans F., Hubert-Delplace A. M., 1980, A&A, 86, 72
Bessell M. S., 1979, PASP, 91, 589
Blaauw A., van Albada T. S., 1963, ApJ, 137, 791
Bohlender D. A., 1989, ApJ, 346, 459
Bohlender D. A., Monin D., 2011, AJ, 141, 169
Bohlender D. A., Landstreet J. D., Brown D. N., Thompson I. B., 1987, ApJ, 323, 325
Brown D. N., Shore S. N., Sonneborn G., 1985, AJ, 90, 1354
Bychkov V. D., Bychkova L. V., Madej J., 2005, A&A, 430, 1143
Cardelli J. A., Clayton G. C., Mathis J. S., 1989, ApJ, 345, 245
Cohen M., Wheaton W. A., Megeath S. T., 2003, AJ, 126, 1090
Daszyńska-Daszkiewicz J., Szewczuk W., 2011, A&A, 728, 11
Donati J.-F., Semel M., Carter B. D., Rees D. E., Cameron A. C., 1997, MNRAS, 291, 658
Eikenberry S. S. et al., 2014, ApJ, 784, L30
Ekström S. et al., 2012, A&A, 537, 1
Farthmann M., Dreizler S., Heber U., Hunger K., 1994, A&A, 291, 919
Georgy C. et al., 2013, A&A, 558, A103
Grevesse N., Noels A., Sauval A. J., 1996, ASP Conf. Ser., 99, 117
Groote D., Hunger K., 1982, A&A, 116, 64
Harris D. L., III, 1956, ApJ, 123, 371
Hobbs L. M. et al., 2008, ApJ, 680, 1256
Hobbs L. M. et al., 2009, ApJ, 705, 32

Hubeny I., Lanz T., 2011, Astrophysics Source Code Library, record ascl:1109.022

Jerzykiewicz M., 1993, A&AS, 97, 421

Kochukhov O., Makaganiuk V., Piskunov N., 2010, A&A, 524, 1

Krtička J., Janík J., Marková H., Mikulášek Z., Zverko J., Prvák M., Skarka M., 2013, A&A, A18, 1

Krtička J., Mikulášek Z., Lüftinger T., Jagelka M., 2015, A&A, 576, A82

Landolt A. U., Uomoto A. K., 2007, AJ, 133, 768

Landstreet J. D., Borra E. F., 1978, ApJ, 224, L5

Lanz T., Hubeny I., 2007, ApJS, 169, 83

Leone F., Manfre M., 1997, A&A, 320, 257

McNally D., 1965, The Observatory, 85, 166

Monin D., Bohlender D., Hardy T., Saddlemyer L., Fletcher M., 2012, PASP, 124, 329

Nieva M.-F., 2013, A&A, 550, 1

Oksala M. E., Wade G. A., Townsend R. H. D., Owocki S. P., Kochukhov O., Neiner C., Alecian E., Grunhut J., 2012, MNRAS, 419, 959

Perryman M. A. C. et al., 1997, A&A, 323, L49

Peterson D. M., 1970, ApJ, 161

Petit V., Wade G. A., 2012, MNRAS, 420, 773

Petit V. et al., 2013, MNRAS, 429, 398

Piskunov N. E., Kupka F., Ryabchikova T. A., Weiss W. W., Jeffery C. S., 1995, A&AS, 112, 525

Preston G. W., 1967, ApJ, 150, 547

Pyper D. M., 1969, ApJS, 18, 347

Shore S. N., Brown D. N., Sonneborn G., Landstreet J. D., Bohlender D. A., 1990, ApJ, 348, 242

Shultz M., Wade G., Rivinius T., Townsend R., 2014, in Sigut A., Jones C., eds, Bright Emissaries: Be Stars as Messengers Star Disk Phys. Astron. Soc. Pac., London, Ontario, Canada, p. 1

Skrutskie M. F. et al., 2006, AJ, 131, 1163

Solano E., 1998, in Wamsteker W., Gonzalez Riestra R., Harris B., eds, ESA SP-413: Ultraviolet Astrophysics Beyond the IUE Final Archive. ESA, Noordwijk, p. 743

Stibbs D. W. N., 1950, MNRAS, 110, 395

Syfert C. K., Hardie R. H., Grenchik R. T., 1960, ApJ, 132, 58

Thompson G. I., Nandy K., Jamar C., Monfils A., Houziaux L., Carnochan D. J., Wilson R., 1978, Catalogue of Stellar Ultraviolet Fluxes (TD-1). The Science Research Council, UK

Townsend R. H. D., Owocki S. P., 2005, MNRAS, 357, 251

Townsend R. H. D., Oksala M. E., Cohen D. H., Owocki S. P., ud-Doula A., 2010, ApJ, 714, L318

ud-Doula A., Owocki S. P., 2002, ApJ, 576, 413

ud-Doula A., Owocki S. P., Townsend R. H. D., 2008, MNRAS, 385, 97

van Leeuwen F., 2007, A&A, 474, 653

Vink J. S., de Koter A., Lamers H. J. G. L. M., 2000, A&A, 362, 295

Voshchinnikov N. V., Henning T., Prokopjeva M. S., Das H. K., 2012, A&A, 541, 1

Wade G. A., Donati J.-F., Landstreet J. D., Shorlin S. L. S., 2000, MNRAS, 313, 851

Waelkens C., 1991, A&A, 246, 453

Walker G. A. H., Bohlender D. A., Krełowski J., 2000, ApJ, 530, 362

Yakunin I. et al., 2015, MNRAS, 447, 1418

This paper has been typeset from a TEX/LATEX file prepared by the author.